On the Mapping and Wavenumber Resolution of Line-Integral Data for Observations of Low-Mode Internal Tides

BRIAN D. DUSHAW

Applied Physics Laboratory, College of Ocean and Fishery
Sciences, University of Washington, Seattle, Washington

ABSTRACT

Techniques are developed for using line-integral tomography data to estimate the spectra, maps, and energy of low-mode internal-tide radiation; the extension of these techniques to other phenomena is obvious. Sparse arrays of line integrals over paths 300–1000 km long can generally determine the direction of propagation of semidiurnal radiation well, but the magnitude of the wavenumbers is ambiguous because of sidelobes in the spectrum. Both wavenumber magnitude and direction can generally be determined for diurnal internal-tide radiation. Spectra for the semidiurnal and diurnal internal tides are estimated for the region of the Atlantic Ocean between Puerto Rico and Bermuda using data obtained during the Acoustic Mid-Ocean Dynamics Experiment (AMODE) in 1991-2. Simulations of semidiurnal internal-tide radiation consisting of wave packets or highly irregular wave crests are used to show that the line-integral data provide better mapping resolution than point data, but the best results are, of course, obtained when both types of data are used. As a practical example of the formalism of these simulations, maps of M_2 internal-tide variability are derived from the AMODE tomography data. Because the inverse problem is underdetermined with the sparse arrays that are deployed in the ocean, the inverse solution generally underestimates the energy of the radiative field. In the simulations employed here, the energy is underestimated by $33\pm10\%$, but the exact amount by which the energy is underestimated is dependent on the assumptions made for the simulations such as the array geometry and the nature of the tidal variability.

5 September 2002

1. Introduction

Recently, ocean acoustic tomography has enabled the detection of large-scale, low-mode internal-tide waves that retain coherence over distances of at least two thousand kilometers (Dushaw et al. 1995; Dushaw and Worcester 1998). These observations were possible because the line- and vertically-integrating nature of tomography allowed very specific wavenumber and mode components of the complicated internal-wave fields to be observed; an observation by acoustic transmissions between transceivers is an observation by an antenna with highly directional properties. Internal tides that travel great distances from where they are generated, while remaining coherent waves, have also been observed by TOPEX/POSEIDON altimetry (Ray and Mitchum 1996, Ray and Mitchum 1997, Kantha and Tierney 1997, Ray and Cartwright 2001, Dushaw 2002). Many questions concerning these low-mode internal-tide waves remain unanswered, hence further observations of them are necessary. Such observations are presently underway near Hawaii (Pinkel et al. 2000). This paper addresses the capabilities of ocean acoustic tomography arrays in resolving the properties of low-mode internal-tide variability. Justifications for the assumptions involved in determining these capabilities necessarily require some review of previous results, but this paper is not intended as a review paper.

The motivations for understanding the resolution properties of line-integral arrays of course stem from the desire to resolve some of the issues concerning internal tides. It is helpful, therefore, to review some of these issues here. The decay mechanisms of these distant-travelling waves is presently unknown; this decay presumably occurs by such mechanisms as bottom friction or a non-linear cascade to higher wavenumbers (Hendershott 1981). Similarly, the decay scale for the low-mode internal tides is unknown; this scale is apparently O(1000 km) or greater. What is the ultimate fate of these waves? The role of the tides has recently been re-recognized as a possible source of mixing of the abyssal ocean (Munk 1966, Munk 1997, Munk and Wunsch 1998, Egbert and Ray 2000). Internal tides that are scattered from topography are one possible mechanism for this mixing. In the region around the Hawaiian Ridge, for example, a significant portion of the energy that is dissipated there from the barotropic tide (20 GW) radiates away from the Ridge in the form of these low-mode internal waves (Egbert and Ray 2000, Merrifield et al. 2000, Ray and Cartwright 2001, Dushaw 2002); the barotropic and baroclinic tidal energy values are uncertain, however. It is apparent that these waves carry energy, presumably energy that is available to drive mixing, for at least a few thousand kilometers from the Hawaiian Ridge. What is the importance of these waves to deep-ocean mixing relative to the local tidally-induced mixing at coastlines or mid-ocean ridges? It is evident that new observations of these internal-tide waves should focus on their energetics, among other things, for a better understanding of their role in abyssal mixing.

A single tomographic line integral, and an array of such line-integrals, act as antennas for the internal tide (or other large-scale wave phenomena in general). The antenna properties of an array of instruments making point measurements of incident radiation are well known (Urick 1967; Capon 1969; Hendry 1977; Kay and Marple 1981), and there have been several previous discussions of the spatial and wavenumber resolution (i.e., mapping) properties of ocean acoustic tomography (Cornuelle and Howe 1987; Cornuelle et al. 1989; Cornuelle and Worcester 2000). In particular, Cornuelle et al. (1989) examined the mesoscale mapping and wavenumber resolution capabilities, and other properties, of moving ship tomography. The present discussion is thus not altogether new, but it does offer a different view of, and additional theoretical basis for, the resolution properties of tomographic arrays, particularly the resolution of the thermal variability caused by large-scale internal-tide waves.

The first half of this paper discusses the beam patterns of line-integral arrays and wavenumber spectral estimating by beam forming. Large-scale, spatially periodic phenomena incident on an acoustic path will cause large variations in travel times of the acoustic pulses when the wave crests are aligned with the acoustic path. For a tomographic array with many acoustic paths, each acoustic path constitutes a high-directivity element of an antenna. The "directivity" of an antenna element is its directional sensitivity to incident radiation (Urick 1967). For the internal tides, the travel times along acoustic paths measure the *average* thermal variability between acoustic transceivers; the high directivity of a path-integral observation (i.e., an antenna element) arises because most often the incident radiation has wavelengths much less than the acoustic pathlengths. The 15-path tomographic array deployed for the Acoustic Mid-Ocean Dynamics Experiment (AMODE) that was deployed in 1991 in the western North Atlantic (Fig. 1) (Dushaw et al. 1996; Dushaw et al. 1997; Dushaw and Worcester 1998) is used as an example of an array that can be used as a steered antenna for observing mode-1 internal tides. The data from each acoustic path are the harmonic constants (amplitude and phase) of the variability; i.e., we assume that the processes involved (the low-mode internal tides) have single frequencies and white noise so that a harmonic decomposition is appropriate. This assumption is supported by the data obtained by tomography (Dushaw et al. 1995, Dushaw and Worcester 1998) and altimetry (Ray and Mitchum 1996, 1997). The internal tide has at times been described as a narrowband process; however, within the limits of the record lengths that have been obtained, tomographic observations record the mode-1 internal tide as a single-frequency process (with the tide consisting of multiple consitutent frequencies, of course.) The beam forming techniques will be applied to harmonic constants obtained from line-integral data to estimate wavenumber spectra of internal-tide radiation.

It is not necessary for the incident radiation to be composed of single discrete wavenumbers for it to be reasonably observed using line-integral methods. In the second half of this paper, the

line-integral observations are used to show that accurate maps of the internal-tide field can be con-structed using an objective mapping technique, which in the present case is equivalent to weighted least squares. Spectral estimates, i.e., periodograms, similar to those obtained from beam forming techniques are also obtained from the objective mapping, with the advantage that they are also vari-ance preserving. Tidal fields consisting of wave packets are simulated using selected wavenumbers. The complicated baroclinic tidal radiation from the Hawaiian Ridge predicted by a model for inter-nal tides (Holloway and Merrifield 1999; Merrifield et al. 2000) are used here as a basis for the sim-ulated tidal fields. Six-path tomographic arrays similar to those that were deployed in 2001 as part of the Hawaiian Ocean Mixing Experiment (HOME, Pinkel et al. 2000) (Fig. 2) are used to simulate the observation of complicated tidal fields; the work described in this paper was used as an aid to designing the geometry of those arrays. While the line-integral observations are used to construct accurate maps of the internal-tide fields, they do not resolve the amplitude and phase of individual wavenumbers well when the tidal field is composed of many wavenumbers and the array is sparse. These techniques for mapping the internal-tide radiation are applied to the AMODE tomographic data. The paper concludes with a discussion of the accuracy to which energy density can be derived from the mapped internal-tide field.

2. Beam pattern of a continuous line array

The beam pattern of a continuous line array, together with beam patterns of arrays and array steering, are described in detail by Urick (1967). These results are reviewed here in the context of the application of arrays of line-integral observations, i.e., measurements along acoustic paths, to observing internal-tide radiation. Since beam forming techniques for tomographic arrays are not well known, this review appears warranted.

The response of an east-west line array of length L to radiation with wavelength λ and inci-dent azimuthal angle θ is

$$v_0(\theta, \lambda) = \frac{\sin[(\frac{\pi L}{\lambda} \sin(\theta - \frac{\pi}{2})]}{(\frac{\pi L}{\lambda}) \sin(\theta - \frac{\pi}{2})} \tag{1}$$

where the subscript "0" means that the response has been normalized to unit amplitude and the phase has been omitted. The beam pattern of the line array is the square of this expression. Figure 3 shows several beam patterns superimposed on a tomography array with paths of length 275, 450,

and 510 km ; as the lengths of the paths get longer relative to the wavelength, the beam patterns narrow. An incident wavelength of 150 km was assumed for these beampatterns; this nominal wavelength for semidiurnal, mode-1 internal tides may be derived from ocean atlas or hydrographic data. By causing displacement of the water column, mode-1 internal tides generate sound speed fluctuations with this wavelength. If the line array is oriented at an angle q with respect to the eastward direction (positive anticlockwise), the normalized response is

$$v_0(\theta, \lambda) = \frac{\sin[\frac{\pi L}{\lambda} \sin(\theta - q - \frac{\pi}{2})]}{(\frac{\pi L}{\lambda}) \sin(\theta - q - \frac{\pi}{2})} \tag{2}$$

The derivation of this equation provides insight into its meaning. Let { $\mathbf{x_n}$ } denote the locations of the tomographic transceivers with respect to an arbitrary origin. The pth path is identified with the path from $\mathbf{x_n}$ to $\mathbf{x_m}$ as $p = \{ 1\ 2\ 3\ ....\}$ with $(n, m) = \{ (1,2)\ (1,3)\ (1,4)\ ...\}$. Suppose the sound speed field is given as (the real part of)

$$c(\mathbf{x}, t) = A\ e^{i(\omega t + \mathbf{k} \cdot \mathbf{x} + \phi)} \tag{3}$$

Here A is the amplitude of the tide wave, ω is its frequency, $\mathbf{k}$ is its wavenumber ($\mathbf{k} = (k \cos\theta, k \sin\theta)$, where θ is the direction of incidence of the radiation measured positive anticlockwise with respect to the eastward direction), and ϕ is its phase. It is assumed that the depth dependence of the sound speed, $c(\mathbf{x}, t)$, is given by the first internal-tide mode; the depth dependence will be omitted here. Prior tidal analyses of the data are assumed, so the time dependence will also be omitted. The line average between $\mathbf{x_n}$ and $\mathbf{x_m}$, or the response of the array element, is

$$v_p(\theta_0, \lambda) = \frac{A}{|\mathbf{x_n} - \mathbf{x_m}|} \int\limits_{\mathbf{x_n}}^{\mathbf{x_m}} e^{i(\mathbf{k} \cdot \mathbf{x} + \phi)} ds \tag{4}$$

where θ_0 is the direction of propagation of the incident radiation with wavelength λ (we assume only one wavenumber is present). The angle of the path with respect to the horizontal is given as

$$q = \text{atan}(\frac{y_m - y_n}{x_m - x_n}) \tag{5}$$

for $\mathbf{x_n} = (x_n, y_n)$. The position of the pth element is taken as the midpoint of the line segment at location $\mathbf{p} = (\mathbf{x_n} + \mathbf{x_m})/2$. Thus, (4) can be written as

$$v_p(\theta_0, \lambda) = A\, e^{i(\mathbf{k}\cdot\mathbf{p}+\phi)} \left(\frac{1}{|\mathbf{x_n} - \mathbf{x_m}|} \int_{\mathbf{x_n}-\mathbf{p}}^{\mathbf{x_m}-\mathbf{p}} e^{i\mathbf{k}\cdot\mathbf{x}} ds \right) \tag{6}$$

The quantity in parentheses gives (2), so $v_p = Ae^{i(\mathbf{k}\cdot\mathbf{p}+\phi)}v_0$.

Another interpretation of these beam patterns is evident when one considers that the line-integral observation is a box-car filter along one dimension and delta function filter in the other dimension. The box-car filter in physical space gives a sinc function filter in wavenumber space along one dimension (Fig. 3). The projection of this filtering property onto wavenumbers of fixed magnitude, such as those for semidiurnal internal tides, gives the beam patterns.

It will be assumed that $v(\theta, \lambda)$ is for a particular frequency. In other words, it will be assumed that a Fourier transform, tidal analysis (Schureman 1958), or complex demodulation is performed on the observed variability, so that the amplitude and phase at the tidal frequencies, ω, have been determined. For the p-th acoustic path, the measured response is therefore just the harmonic constants, or

$$v_p(\theta_0, \lambda, \omega) = A_p e^{-iG_p} \tag{7}$$

where A_p and G_p are the amplitude and phase of the observed variability on the pth path at frequency ω. The tidal analysis offers a large gain in signal-to-noise ratio, such that the subsequent spectral analysis offers better results than can be achieved by other means such as, for example, "high-resolution frequency wavenumber spectrum analysis" (Capon 1969).

3. Beam forming with an array of continuous line integrals

Urick (1967) discusses beam patterns of arrays and array steering in detail, except for arrays of line-integrating "instruments". By way of introduction to the array processing with line-integral

data and to notation, the beam pattern and beam forming of an array of nondirectional elements (i.e., instruments at single points such as thermisters) will be discussed first. We will use u_j to refer to the response of nondirectional (point) instruments, and v_j to refer to the response of directional (line-integral) "instruments". The beam pattern of an array is the sum of the responses of each element in the array to incident radiation with a given wavenumber. Beam forming is the process of calculating the beam pattern with the addition of phase shifts that would arise from incident radiation to each element's response. If radiation at a particular wavenumber is present, then all elements add coherently for phase shifts equal to but opposite in sign to that given by the incident wavenumber. This coherent response shows the wavenumber content of the radiation, or the wavenumber spectrum.

a. Point measurements

Because the normalized beam pattern for a nondirectional element is unity, the response of an array of N nondirectional elements is

$$U(\mathbf{k}) = \sum_{j=1}^{j=N} 1 \cdot A\, e^{i(\mathbf{k}\cdot\mathbf{p_j} + \phi)} \tag{8}$$

The $\mathbf{p_j}$ are the locations of the elements with respect to an arbitrary origin. The beam pattern is given as

$$B(\mathbf{k}) = U(\mathbf{k})U^*(\mathbf{k}) = \sum_{i=1}^{i=N} \sum_{j=1}^{j=N} A^2\, e^{i\mathbf{k}\cdot(\mathbf{p_j} - \mathbf{p_i})} \tag{9}$$

Consider the array of nondirectional elements as described in Fig. 1. The elements of this array are located at the midpoints of an array of line elements, so that there are as many point elements as line elements, which will be considered below. The beam pattern for the array of nondirectional elements is shown in Fig. 4a. The sidelobes of the pattern indicate the wavenumbers for which the elements of the array add coherently, and thus they represent ambiguities in the determination of the wavenumber of incident radiation.

Now suppose that radiation $r(\mathbf{x}) = e^{i\mathbf{k_0}\cdot\mathbf{x}}$ of a fixed wavenumber $\mathbf{k_0}$ is incident on the above antenna. This field has unit amplitude and zero phase. The response of each element u_j is given by the individual terms of (8) (plus noise, which we neglect for the time being), i.e., $u_j = e^{i\mathbf{k_0}\cdot\mathbf{p_j}}$. The

array can be made to sum coherently (boosting the signal-to-noise ratio) if the array is "steered" by introducing appropriate phase shifts, that is,

$$U(\mathbf{k}) = \sum_{j=1}^{j=N} u_j e^{-i\mathbf{k}\cdot\mathbf{p_j}} \tag{10}$$

The steered beam pattern, which is UU^*, will be the beam pattern of Fig. 4a shifted so that the central peak lies at $\mathbf{k} = \mathbf{k_0}$. Note that

$$UU^* = B(\mathbf{k}) = \sum_{j=1}^{j=N} \sum_{l=1}^{l=N} u_j u_l^* e^{-i\mathbf{k}\cdot(\mathbf{p_j}-\mathbf{p_l})} \tag{11}$$

which is also an estimate of the wavenumber spectrum. The spectral estimate is at the frequency for which the u_j were determined.

b. Line-integral measurements

The array of line-integrating elements has very different antenna properties; these properties have not been well described in the literature. Each element of an array of continuous line measurements has the normalized response $v_{0\,j}$, given by (2); hence from (6) the unsteered response of an array of continuous line measurements is

$$V(\mathbf{k}) = \sum_{j=1}^{j=N} v_{0\,j}\, A\, e^{i\mathbf{k}\cdot(\mathbf{p_j}+\phi)} \tag{12}$$

The beam pattern is again $B(\mathbf{k}) = V(\mathbf{k})\,V^*(\mathbf{k})$. Figure 4b shows the beam pattern for the array of continuous line elements depicted in Fig. 1. The beam pattern indicates that the elements of the array sum coherently only for near-zero wavenumbers. Fundamentally, this results from the high directivity of the elements. Because each element is generally sensitive only to wavenumbers in certain directions for incident wavelengths comparable to or less than the length of the line elements, the elements of the array can add coherently only for near-zero wavenumbers.

For radiation incident on the array, the response measured at each element is

$$w_j(\mathbf{k_0}) = v_{0\,j}e^{i\mathbf{k_0}\cdot\mathbf{p_j}} \qquad (13)$$

where v_{0j} is given by (2) for $\mathbf{k} = \mathbf{k_0}$ and the jth element is located at $\mathbf{p_j}$. As measured, this response is the amplitude and phase of the tide, or

$$w_j = A_j e^{-iG_j} \qquad (14)$$

The steered response of the array is

$$V(\mathbf{k}) = \sum_{j=1}^{j=N} w_j v_{0\,j}(\mathbf{k})e^{-i\mathbf{k}\cdot\mathbf{p_j}} \qquad (15)$$

where the directionality of each element is accounted for using the weights $v_{0\,j}(\mathbf{k})$ given by (2). The weight $v_{0\,j}(\mathbf{k})$ is a wavenumber filter that removes all wavenumbers (for wavelengths smaller than the path length) that are not nearly perpendicular to the j-th path. Note that given the directionality of each element, the array can never be steered so that all elements sum coherently. Only those elements that are very nearly parallel to each other can be made to sum coherently. As an example, Fig. 5a shows the "steered" beam pattern, or spectral estimate, $B(\mathbf{k}) = V(\mathbf{k})V^*(\mathbf{k})$, derived from (14) and (15) given radiation with wavenumber $(0, 2\pi/150)$ rad/km incident on the array (and no noise). The figure shows that while the direction of incidence is well determined, the magnitude of the wavenumber is determined only to within a set of sidelobes. For the example considered, only approximately two elements contribute to determining the wavenumber; hence there is considerable aliasing, or considerable sidelobes, of meridional wavenumbers. In any particular direction, most of the elements of the array are blind owing to the narrow beam patterns of those elements, but generally an array such as that depicted in Fig. 1 will have a few elements that are sensitive to any particular direction. Because none of the acoustic paths are oriented exactly zonally, the ridge of side lobes in Fig. 5a does not lie exactly along the meridian.

The first mode of the diurnal internal tide has a wavelength of 400–500 km. Some of the acoustic paths of Fig. 1 are shorter than this wavelength, and thus their response to this radiation is more like that of nondirectional elements. Figure 5b shows the steered beam pattern for a wave with wavenumber $(0, 2\pi/400)$ rad/km incident on the array (and no noise). For this longer wavelength both the direction and the magnitude of the incident wavenumber are resolved.

The simulated spectral estimates are surprisingly similar to the actual spectral estimates at semidiurnal and diurnal frequencies (the diurnal spectra have been described by Dushaw and Worcester (1998)) for internal-tide variability in the western North Atlantic (Figs. 5c and 5d). It is evident that several wavenumbers are present in the actual spectra, which may acount for the large responses at near zero wavenumber in the semidiurnal case. This complicated wavenumber content is not surprising in the real ocean. Internal-tide radiation is evidently incident on the tomographic antenna from several directions. The presence of several wavenumbers complicates the spectral estimation, as will be described in the next section.

4. Sensitivity of spectral estimates when multiple wavenumbers are present

Because spectral estimation is fundamentally a modeling problem (Kay and Marple 1981), it is inherently problematic to use any observing array to estimate spectra when more than one wavenumber is present. A classic example of this problem is a standing wave (two wavenumbers of equal magnitudes and in opposite directions) for which the detectors lie on the nodes of the wave. In this example, no energy will be detected at the two wavenumbers that are present. Spectral estimation using line-integral data when multiple wavenumbers are present is similarly problematic. Because the averaging on most of the acoustic paths gives only a small signal, i.e., the paths detect only a fraction of a wavelength, the observed amplitudes and phases of the various waves can easily be distorted by interference. In this way, the estimated spectra can also be distorted.

An example of a spectral estimate that has been distorted by the presence of multiple wavenumbers can be found in the spectral estimate reported by Dushaw and Worcester (1998) for internal-tide waves at diurnal frequency. The observed tidal variations were interpreted as standing waves, yet the estimated spectra (Fig. 5d) do not show a clear presence of two equal and opposite wavenumbers as might be expected. However, there is evidence in the estimated spectrum of additional wavenumbers, particularly a tidal propagation to the southeast. A simulation shows that when three wavenumbers are present (two wavenumbers for a standing meridional wave and a wavenumber for a wave with smaller amplitude propagating to the southeast) the estimated spectra are indeed distorted. The resulting spectra are sensitive to the *phase* of the smaller-amplitude wave (Fig. 6). The smaller-amplitude wave can influence the phase observed on each of the line integrals sufficiently enough to influence the spectral estimation. In this case, the amplitude of the waves and direction of the wavenumbers present may be somewhat ambiguous, but the magnitude of the wavenumbers present appears to be robust.

To emphasize that spectral estimation is a modeling problem, note that the diurnal waves are not simple sinusoids as has been assumed for these spectral estimates. Near the critical latitude for

diurnal waves (30°N), the variation of the waves in the meridional direction is described by Airy functions (Hendershott 1981, Dushaw and Worcester 1998). Spectral estimation using Airy functions, rather than sinusoids, is not discussed in this paper, but for our purposes the sinusoid approximation is adequate.

5. Observing wave packets of outgoing radiation

The sensitivity of the line-integral observations to particular wavenumbers suggests that suitably designed arrays can be used to observe tidal radiation that consists of wave packets rather than monochromatic waves which are rare in nature. Using a primitive-equation ocean model forced by the barotropic tides, Merrifield et al. (2000) found a complicated internal-tide field emanating from the Hawaiian Ridge. The simulated sea surface height determined from the model results (Fig. 2) was similar to that determined from TOPEX/POSEIDON altimetry data (Ray and Mitchum 1996, 1997; Dushaw 2002). The output of this model for internal tides could be used as a basis for examining the ability of the sparse line-integral data to detect, or map, "realistic" tidal radiation from a topographic feature, but the study discussed here requires a tidal field over a domain that is larger than can be feasibly employed for the ocean model. However, it is straightforward to simulate tidal fields similar to those resulting from the model, thus giving the simulations a reasonably physical basis.

Given the discussion in the preceding sections, the geometry of the array that can best observe radiation that is propagating in some general direction is evident. The best wavenumber resolution will be obtained when using paths that are oriented almost parallel to the expected general orientation of the wave crests. Such an array employing four moorings has a delta geometry; this is the basic geometry employed for the HOME experiment (Fig. 2). The geometry used for the simulations described here is a triangular array with a central mooring. The diamond-shaped array deployed for HOME evolved from the simulation array; it has identical wavenumber resolution as the simulation array. For the HOME array, the central mooring was flipped outside the triangle to a point of equal distance from the base of the triangle to create a quadrilateral array. The shortest path of the HOME array is about three times longer than that of the simulation array, and the HOME array covers a little more area. In addition to the line-integral data, point data are obtained from the simulated tidal fields at the vertices of the array. Point data such as these may be obtained by thermisters on each of the tomography moorings.

A description of the properties assumed for the simulated tidal fields will be given first, followed by a discussion of the modeling assumptions that will be used in mapping the fields. The results of this mapping exercise are then described. Henceforth, the simple beam forming

techniques used to introduce the properties of the line integrals are abandoned in favor of the objective map approach.

a. Simulation of the tidal field

The general characteristics of the tidal field derived from the primitive-equation model can be easily simulated. Wavenumber spectra estimated from TOPEX/POSEIDON altimetry (Ray and Mitchum 1997) are not expected to be reliable for these purposes because of the weak signal to noise and sampling properties of the altimetry, and the wavenumber resolution of the spectra estimated from the numerical model of Merrifield and Holloway (2000) (Fig. 2) is limited by the small size of the model domain. Therefore, an analytical spectrum is assumed for these simulations. A set of semidiurnal wavenumbers (with wavelengths near 150 km) with directions roughly within 15 degrees of north will be used to simulate the field. A spectrum for these wavenumbers will be peaked on the meridional wavenumber with a rapid falloff away from the semidiurnal wavenumber. The assumed spectrum is given by

$$S(\mathbf{k}) = \sum_{j=1}^{j=3} W_j \exp[-(\mathbf{K_j} - \mathbf{k})^2/(2\,K_0^2)] \tag{16}$$

where $W_j = \{0.85, 0.6, 0.6\}$ gives the weights assigned to the wavenumbers, $|\mathbf{K_j}| = 2\pi/150$ km, $\mathrm{ang}(\mathbf{K_j}) = \{90°, 75°, 105°\}$, and $K_0 = 0.2\,|\mathbf{K_j}|$ (Fig. 7). The peaks of this *ad hoc* spectrum have a finite width because of the assumption that the wavenumbers of an actual tidal field will not all be the exact wavenumber predicted by theory. The width of the tidal spectrum in wavenumber space may in some circumstances be related to the width of the tidal lines in frequency space through the dispersion relation. The lines in the frequency spectra for internal tides observed by long-range acoustics are quite narrow. Time series have not yet been obtained with sufficient quality and record length to measure this line width. However, using tide-gauge data obtained around Hawaii Munk and Cartwright (1966) and Ray and Mitchum (1997) have described "tidal cusps," or weak tidal energy at frequencies adjacent to the main spectral lines of the barotropic tide, that might be caused by internal tides. The narrow width of the lines in the frequency spectra for internal tides implies that the wavenumbers employed for the inversion should be closely confined to the theoretically allowed wavenumbers of the internal tide. For observations near the topography where the tide is generated, however, it is not clear if this strong assumption is justified. For the purposes of these simulations, therefore, the finite spectral line width described by (16) will be assumed. The conclusions given below are necessarily dependent on the assumptions used for these simulations

and for the inversion. Stronger assumptions, such as very narrow spectral peaks, would result in stronger conclusions, if those assumptions were true.

The phases of these wave components are randomized using values in a 35-degree bin centered on a single value in order to simulate the likelihood that the internal tides generated along the Hawaiian Ridge have roughly the same phase. Figure 8 shows three examples of the simulated field. These examples may be compared with the results of Merrifield et al. (2000) (Fig. 2). The simulated tidal fields have an oscillatory covariance in the meridional direction, because the tide is radiating in that direction, and a slowly decaying covariance in the zonal direction. In addition, an *ad hoc* white noise that is 20% of the rms of the tidal variability was added to each grid point of the simulation. This noise level is meant to allow for noise in the data from internal waves or from internal-tide variability of higher modes. The grid spacing for these simulations is 10 km.

b. Modeling assumptions

An obvious goal for the inversion of the harmonic constants obtained by the observing array is to obtain an accurate objective map of the tidal field. The forward problem and penalty function used for this inversion are given in the appendix. With the data and model weight matrices assumed here, the inverse is identical to weighted least squares (Munk et al. 1995). The inversion must assume an *a priori* covariance for the model parameters. The best covariance is naturally one that is as similar to the true covariance as possible, i.e., a set of generally meridional wavenumbers with magnitudes appropriate for the semidiurnal internal tide. Given that the data are the amplitude and phase for a particular tidal frequency, the assumption that the modeled wavenumbers are close to the theoretically expected wavenumber results in a map for the tidal field that is consistent with the dispersion relation for these waves. It is a good assumption that large-scale waves are propagating in a linear fashion according to their dispersion relation (when they are observed at distances greater than several wavelengths from their region of generation), so that more sophisticated modeling, such as data assimilation using a primitive-equation model, is not obviously necessary.

The best covariance to use in an inversion can rarely be derived from the available data, so an *a priori* covariance must be constructed based on general notions of oceanographic variability (Bennett 1992, Munk et al. 1995). For most of these simulations we will assume that the covariance is the diagonal of the true covariance (i.e., the model parameters are independent, which is certainly not true). This diagonal is also the spectrum (Fig. 7), and it specifies the weighting assigned to each wavenumber. If the assumed and "true" covariances differ significantly, poor solutions will be obtained for the tidal field . However, the purpose here is to examine the ability of sparse arrays to map the tidal field, not the ability of physical oceanographers to construct accurate *a priori* covariances.

5 September 2002

The line-integral data are assumed to have an uncertainty of about 2%, and the point data are assumed to have an uncertainty of 20%. These assumptions are roughly in accordance with our experience with real data (Dushaw et al. 1995, 1997).

c. Results

If both line-integral and point data are used, the objective map of the internal-tide field is similar to the true fields in the region for which data are available (Fig. 9). The solution naturally decays to zero away from regions where data are available. In general, the tidal amplitudes of the inverse solution are underestimated, as will be discussed further below.

The error map resulting from the inversion shows that the rms uncertainty in estimating the tidal field within the observing array is about 20–40%, and this uncertainty increases to 100% for those parts of the map more than about 100 km away from the array (Fig. 10). Note that the error maps do not have oscillatory characteristics because both components (amplitude and phase) of the tide are observed. A comparison of the error maps when only point data, or only line-integral data, are used in the inversion shows that the line-integral data do better at mapping the tidal field within the array than the point data do; this conclusion will be examined further later.

The sensitivity of the inverse map to the *a priori* spectrum can be examined by assuming different *a priori* spectra. Two examples of other possible spectra are a broad $|\mathbf{k}|^{-2}$ spectrum (commonly assumed for objective maps) and a set of semidiurnal wavenumbers in the meridional direction that is more focused than the "true" spectrum (Fig. 11). In both cases, the solution for the field agrees with the data, but the modeling assumptions closest to "truth" naturally result in better solutions for the tidal field. Note that the narrowest *a priori* spectrum gives the most oscillatory solution, particularly in regions some distance away from the locations of the observations.

With the framework described above, we can examine the ability of arrays of various sizes and shapes to resolve the field. A four-mooring array, equilateral with 500-km sides, was scaled in the meridional and zonal directions to determine which size and shape minimized the misfit between "true" and estimated tidal fields. Three cases were considered: (1) the set of four measurements at the points of the moorings, (2) the set of six line-integral measurements, and (3) the set of both line-integral and point measurements. The number of data are twice the number of observations because both amplitude and phase are derived from each measurement. The criterion for deciding the "best" array is somewhat ambiguous. Small arrays do better at resolving a small area of the tidal field, while the inhomogeneity of the field makes it necessary that some substantial area be mapped in order to gain a better understanding of the properties the tidal field. The measure of the goodness of fit assumed here is the mean-square misfit between the inverse solution for the field and the "true" field over a region that is circular, 400 km across, and centered on the array.

Although this criterion is arbitrary, it reflects the basic goal of resolving the tidal field over a domain that is a few tidal wavelengths across. To calculate the average mean-square misfit, objective maps of 500 simulated tidal fields were made (Fig. 12), although these results could also be calculated directly from the error maps. These 500 maps were made for each of the three cases described above and several meridional and zonal scalings of the basic equilateral array.

When only the point data are available, the best maps are obtained using an equilateral triangle with 250-km sides (Fig. 12a). As expected, for the line-integral data alone, the best maps are obtained when the meridional scaling is 0.5−0.6 and the zonal scaling is 0.8−1.0, i.e., a triangle with a base length of 400−500 km and a height of around 200 km (Fig. 12b). The mapping ability of the array of point measurements is not as good as that of the array of line integrals. The mean-square misfits between "true" and estimated tidal fields are consistent with the maps of uncertainty calculated by inverse theory (Fig. 10).

d. Discussion

The inverse solution is a biased estimator in that it roughly uses the minimum possible square of amplitudes required to obtain a fit to the data consistent with uncertainty, i.e., the inversion fits the data by determining phases for the various waves such that the square of wave amplitudes are minimized. The solution produces minimum energy (and hence amplitudes) by design. Given that the inverse problem is underdetermined, it is not surprisingly that the skill in resolving individual wavenumber amplitudes is poor (Fig. 13). For mapping purposes, however, it is overly stringent to require that an observing array resolve the amplitudes of individual wavenumber with good skill; this requirement was adopted by Cornuelle, et al. 1989. It may be tempting to abandon the biased estimator used for the objective map in order to obtain wavenumber amplitudes that result in greater energy, but fitting data to a model by unweighted least squares methods is not desirable. One might also build phase relations into the *a priori* covariance, if something is known about the phases of the wavenumbers. Such assumptions about the phases may be too strong to be acceptable, however, and in the present case it proves to be an ineffective remedy. If the true covariance is assumed for the the *a priori* weighting of model parameters, the sparse array considered in these simulations has only slightly better skill at resolving the model parameters. Given the sparseness of the observing array, therefore, we should be concerned here not so much with the resolution of the individual wavenumbers, but with the ability of a model consisting of a few wavenumbers to resolve a highly anisotropic tidal field over a limited area.

Even if the spectrum of the "true" field is broadly peaked about some single wavenumber, reasonable maps over a domain of interest, e.g., the 400-km-diameter area assumed in the foregoing discussions, can be obtained with a model that consists of only a few wavenumbers. Such a model

appears to be adequate for mapping, even though the true spectral content of the field is unknown beyond the general assumptions that (a) semidiurnal wavenumbers dominate and (b) the field is anisotropic, with most of the radiation coming from some general direction. If the tidal field is sufficiently complicated, however, the data from the observing array may perfectly resolve the few wavenumbers used in the inversion, yet give poor maps.

The more select the set of wavenumbers assumed for the inversion, the more oscillatory the solution will be inside and outside of the domain in which measurements are available. The more oscillatory solution may allow a better prediction of the tidal variability outside the experiment domain. A sharply peaked *a priori* specrum is a strong assumption, however, and if that assumption is incorrect, the accuracy of the solution away from the location of the measurements will quickly deteriorate. The ability of these objective maps to resolve the tidal field away from the locations of the measurements is similar to the ability of quasigeostropic models to predict variability before or after the time of observations. The prediction skill decays as the difference between time of prediction and time of measurement increases (Cornuelle and Worcester 2000).

To verify the anisotropy of the field, it may be important to design an array with paths that are sensitive to radiation from directions where it is not expected. This goal would suggest a wider array that would sacrifice resolution for greater directional coverage.

Wavenumber spectra, or periodograms, can be estimated using the objective mapping approach described above, if all wavenumbers are used for the model and these wavenumbers are given equal weight so that the spectrum is not prejudiced. Such spectral estimates were found to be nearly identical to the beam forming spectral estimates discussed earlier. Unlike the beam forming spectral estimates, however, the spectral estimates obtained by inverse methods are variance preserving. In addition, the inverse approach also gives an estimate of the uncertainty in the spectrum. The beam patterns associated with the beam forming spectral estimates suggest that there are regions of the spectrum where an observing array may have poor skill. Examples of spectral estimates derived from objective maps will be given in the next section.

6. An Application: Maps of AMODE tomography observations of internal tides

The approach described in the previous section for mapping internal-tide fields has been applied to the observations of internal-tide variations during AMODE. These techniques were also employed for mapping TOPEX/POSEIDON altimeter data near Hawaii (Dushaw 2002).

The diurnal internal tides observed during AMODE (Fig. 1) have been described by Dushaw and Worcester (1998). The acoustic travel times were used to derive time series of the amplitude of the first internal-wave mode on each of the 15 acoustic paths. The time series were then high-pass

filtered by subtracting daily averages. Tidal analyses of the time series for each acoustic path then gave harmonic constants for the dominant eight tidal constituents (Dushaw et al. 1995); the record lengths were 200−300 days. Since the tidal analyses accounted for 40−70% of the variance of the time series of mode amplitude, it is clear that the observed variations caused by internal tides were temporally coherent, and they were obviously spatially coherent because the signals appeared in the line-integral measurements on paths up to 670 km long. The harmonic constants for the M_2 constituent are used here to derive a map of the mode-1 amplitude (Fig. 14a). In this map, the cosine component of the tidal field appears to be propagating northwest−southeast, while the sine component of the tidal field (right) is significantly stronger and propagating meridionally. These properties appear to result from the chance location of the acoustic paths, such that the two zonal paths, for example, happen to detect a wave with phases near 90° or 270°. The separation of the parallel paths of the tomographic array was about 1.5 semidiurnal wavelengths, also by chance. Propagation of M_2 internal tides to the southeast in this region has been reported by Hendry (1977), and the strong amplitude for meridional wavenumbers is similar to the diurnal internal tide variability that has been observed by the AMODE tomographic array (Dushaw and Worcester 1998).

For Fig. 14a, the *a priori* wavenumber spectrum was assumed to be peaked on the semidiurnal wavenumber, as for the simulations described above, except that an omnidirectional *a priori* spectrum (Fig. 14b) was used. The amplitudes of the wavenumbers derived from the objective map give an estimate of the wavenumber spectrum, although this spectrum has only semidiurnal wavenumbers by assumption. The spectrum shows that meridional or northwest-southeast wavenumbers dominate, as suggested by the maps themselves. The direction of propagation can be determined, but with 180° ambiguity. As a result, the solution that minimizes the variance of wavenumber amplitudes is a field of standing waves, that is, a biased estimator will model an observed wave of amplitude *A* using a standing wave consisting of two waves of amplitude *A*/2 because $A^2 > 2(A/2)^2$.

7. Array design for measuring the average energy of outgoing radiation

If the array is designed for the purpose of making the best estimate of the baroclinic tide energy or energy flux, perhaps an array designed for the best resolution of a map of the tide over an area may be less than optimal. Rather, it may be possible to design an array specifically for resolving the net energy or energy flux. The net energy flux is the energy density times the group velocity. Net flux defined this way is the net energy transported by all waves, rather than the energy flux across any particular boundary. Some caution must be exercised when calculating energy flux this way when multiple wavenumbers are present. In the extreme example of a standing wave consisting

of two opposing wavenumbers, there is energy density but no net energy flux. The most accurate energy flux estimates will be made when the dominant wavenumbers present are distingished, insofar as that is possible. As will be shown next, the net energy density is proportional to the sum of the squares of the amplitudes for the wavenumbers; this is the Parceval theorem.

The time-averaged potential energy density of mode-1 internal waves is

$$PE = \tfrac{1}{2} \int_D^0 \rho(z)N^2(z)\langle \zeta^2(\mathbf{x}, z, t)\rangle_{\text{time}} dz \qquad (17)$$

Where $\rho(z)$ is the density, $N(z)$ is the buoyancy frequency, and $\zeta(\mathbf{x}, z, t)$ is the displacement. The displacement of mode-1 waves is modeled as

$$\zeta(\mathbf{x}, z, t) = \sum_j C_j f(z) \cos(\omega t + \mathbf{k_j} \cdot \mathbf{x} - \phi_j) \qquad (18)$$

where $f(z)$ is the first vertical mode for displacement calculated from density. Since the ratio of potential energy to kinetic energy is $r = (\omega^2 - f^2)/(\omega^2 + f^2)$, the total energy (potential + kinetic) follows directly as $E = (1 + 1/r)PE$, or

$$E = \frac{r+1}{2r} \int_D^0 \rho(z)N^2(z) \left\langle \left(\sum_j C_j f(z) \cos(\omega t + \mathbf{k_j} \cdot \mathbf{x} - \phi_j)\right)^2 \right\rangle_{\text{time}} dz \qquad (19)$$

In the time average of the cosines, the spatial variation drops out and a factor of a half results, so that

$$E = \left(\frac{r+1}{4r} \int_D^0 \rho(z)N^2(z)f^2(z)dz \right) \sum_j C_j^2 \qquad (20)$$

The energy density, therefore, is proportional to the sum of the squares of the amplitudes for the wavenumbers; all other terms can be calculated using hydrographic or climatological data. The sum of the squared amplitudes is precisely the quantity that is minimized by the objective map.

5 September 2002

If the goal of an experiment is to measure the net tidal energy density or flux, the design criterion may not necessarily be for the best resolution of individual amplitudes. Rather, one could choose the far more limited criterion that the sum of the square of the amplitudes be as close to truth as possible. However, this approach is moot because the poor skill of sparse arrays in resolving wavenumbers results in a gross underestimation of the amplitudes of the wavenumbers. For the previous simulations, the energy calculated by summing the squares of the wavenumber amplitudes given by the inverse solution was typically a mere 1−2% of the "true" value. The bottom line is that although the true and estimated physical-space maps are quite similar in the region of the observing array, the inverse solution for the sum of the squares of the wavenumber amplitudes is miniscule compared to the true sum.

A better approach to determining the ability of an array to measure the average energy is to average the square of the solution for the amplitude of the tidal field over an area, rather than over time. The energy derived from an inverse solution will generally be less than the true energy, however, because a biased estimator is employed. One sensible approach is to average over the entire domain using spatially dependent weighting derived from the uncertainty of the inverse map such that the energy is weighted more in regions of small uncertainty and less in regions of large uncertainty. One such approach is

$$\langle \zeta^2(\mathbf{x}, z, t) \rangle_{\text{time}} = \langle \zeta^2(\mathbf{x}, z, t) \rangle_{\text{area}} = \int \int_{\text{area}} W(\mathbf{x}) \, \zeta^2(\mathbf{x}, z, t) \, dx \, dy \tag{21}$$

The weighting, $W(\mathbf{x})$ is

$$W(\mathbf{x}) = \frac{1}{R} \left[\max(E(\mathbf{x})) - E(\mathbf{x}) \right] \tag{22}$$

where $E(\mathbf{x})$ is the uncertainty map, and R is a normalizing factor given by

$$R = \int \int_{\text{area}} \left[\max(E(\mathbf{x})) - E(\mathbf{x}) \right] dx \, dy \tag{23}$$

For the array geometries and modeling assumptions used in the simulations, the energy derived using (21) is smaller than the "true" energy by 33±10%, where the uncertainty is determined from the rms of energy misfit for the 500 realizations employed in section 5. It is probably acceptable that the energy is underestimated by 33%, given the difficulty of making observations in the ocean. Some correction can probably be made for the underestimation of energy.

7. Conclusions

Given the considerable uncertainty in the energy carried by both low- and high-mode internal tides, there is a need to better study internal tides and their role in making energy available for ocean mixing. One motivation for this work has been to prepare for the deployment of the HOME tomography arrays in 2001 for observing the internal tides radiating from the Hawaiian Ridge (Pinkel et al. 2000).

Beam patterns of line-integral arrays show that observations by such arrays are highly directional. Beam forming with a sparse array of highly directional elements shows that the direction of propagation can be well determined, but because of sidelobes in the spectra the magnitude of the wavenumbers present is ambigously determined. The magnitude of the wavenumbers can be determined theoretically, however. Not surprisingly, point arrays have very different spectral characteristics; point arrays have many more sidelobes because they are susceptible to wavenumbers of all magnitudes and directions. More generally, frequency-wavenumber spectra could be derived from the observation of broadband processes (e.g., Zang and Wunsch, 1999) by line-integral data by calculating Fourier transforms of the time series obtained by each element of the observing array, followed by an application of the beam forming techniques used here to obtain a wavenumber spectrum for each frequency band. Spectral estimates by sparse arrays can be easily distorted when more than one wavenumber is present, however. The distortion is partly because of the directivity of the elements, but such distortion is also a problem for any sparse array.

The radiation of realistic, irregular tides of the lowest internal-wave mode was simulated using semidiurnal wavenumbers in some general direction and wavenumber phases that are slightly randomized. Simulations of the observation of those internal tides found that the line-integral observations map the field better than point observations, given an equal number of moorings. The best array for measurements at points is a small equilateral triangle, while the best array for measurements by line integrals is an isosceles triangle with height about half the length of the base. With four moorings, the tidal fields could be mapped with an uncertainty of 20–40%.

The mapping approach was applied to internal tides observed by a tomographic array at both diurnal and semidiurnal frequencies in the western North Atlantic, and a periodogram of the variability was derived. Strong internal tides were found propagating in the meridional direction, probably from the Puerto Rico shelf or trench, and a weaker propagation to the southeast was also found, probably from the Blake escarpment. These tidal observations will be described in more detail in a separate publication (Dushaw, in preparation).

The objective map approach naturally minimizes, hence it underestimates, the energy of the mapped tidal field. When using a sparse observational array the amplitudes of individual

wavenumbers are poorly determined, although the map over the area of observation is accurate. Therefore, the energy is better calculated from the spatial map than from the wavenumber amplitudes. For the simulations employed, the sparse arrays underestimate energy by 33±10%. The exact amount by which the energy is underestimated is dependent on the observing array and the assumptions made about the nature of the tidal variability for the simulations. Observations by sparse arrays generally result in lower bounds for measurements of the energy of internal tides.

Appendix
Sines and Cosines

This appendix describes the forward problem for the mapping exercises given in sections 5 and 6. The notation in complex variables of the text is abandoned because the inverse formalism is problematical otherwise. A time series obtained using either point or line-integral observations is given by

$$\eta(t) = A\cos(\omega t - G) = A\cos(\omega t)\cos(G) + A\sin(\omega t)\sin(G) \tag{A1}$$

The two-dimensional tidal field of mode-1 amplitude may be described as

$$F(x,y,t) = \sum_j C_j \cos(\omega t + \mathbf{k_j} \cdot \mathbf{x} - \phi_j) = \sum_j C_j[\cos(\omega t)\cos(\mathbf{k_j} \cdot \mathbf{x} - \phi_j) - \sin(\omega t)\sin(\mathbf{k_j} \cdot \mathbf{x} - \phi_j)] \tag{A2}$$

The various spectra that may be assumed for the wavenumber components of this field have been described in the text. A line-average measurement of (A2) over a path of length L gives

$$\eta(t) = \sum_j C_j \cos(\omega t)\frac{1}{L}\int \cos(\mathbf{k_j} \cdot \mathbf{x} - \phi_j)dl - \sum_j C_j \sin(\omega t)\frac{1}{L}\int \sin(\mathbf{k_j} \cdot \mathbf{x} - \phi_j)dl \tag{A3}$$

so, by comparison with (A1) above,

$$A\cos(G) = \sum_j C_j \frac{1}{L}\int \cos(\mathbf{k_j} \cdot \mathbf{x} - \phi_j)dl \tag{A4}$$

$$A\sin(G) = -\sum_j C_j \frac{1}{L}\int \sin(\mathbf{k_j} \cdot \mathbf{x} - \phi_j)dl \tag{A5}$$

Note that there are two independent data: either the amplitude and phase of the observations or, equivalently, $A\cos(G)$ and $A\sin(G)$. Expanding (A4) and (A5) and setting $Q_j^c = \int \cos(\mathbf{k_j} \cdot \mathbf{x})$, $Q_j^s = \int \sin(\mathbf{k_j} \cdot \mathbf{x})$ and $X_j = C_j \cos(\phi_j)$, $Y_j = C_j \sin(\phi_j)$, gives

$$\begin{bmatrix} A\cos(G) \\ A\sin(G) \end{bmatrix} = \begin{bmatrix} Q^c & Q^s \\ Q^s & -Q^c \end{bmatrix}\begin{bmatrix} X \\ Y \end{bmatrix} \tag{A6}$$

where the index j has been dropped in favor of matrix notation. Inverse methods can be brought to bear on this equation to solve for $x = \{X, Y\}$ using the data $y = \{A\cos(G), A\sin(G)\}$. Note that the resulting map in physical space has two orthogonal components, one for $A(x,y)\cos[G(x,y)]$ and one for $A(x,y)\sin[G(x,y)]$, and corresponding separate error maps.

5 September 2002

If **P** is the matrix of Q's above connecting the model to data, then the penalty function used for the inverse is

$$J = (y - \mathbf{P}x)^T \, \mathbf{R}^{-1} \, (y - \mathbf{P}x) + x^{\,T}\mathbf{S}^{-1} \, x \qquad\qquad (A7)$$

where $\mathbf{R}^{-1}$ and $\mathbf{S}^{-1}$ are the data and model weight matrices, respectively (Munk et al. 1995). Because this penalty function includes a term to minimize the model parameters, the solution is biased towards zero.

REFERENCES

Bennett, A. F., 1992: *Inverse Methods in Physical Oceanography.* Cambridge University Press.

Capon, J., 1969: High-resolution frequency-wavenumber spectrum analysis. *Proc. IEEE,* **57,** 1408−1418.

Cornuelle, B., and B. M. Howe, 1987: High spatial resolution in vertical slice ocean acoustic tomography. *J. Geophys. Res.,* **92,** 11 680−11 692.

Cornuelle, B., W. Munk, and P. Worcester, 1989: Ocean acoustic tomography from ships. *J. Geophys. Res.,* **94,** 6232−6250.

Cornuelle, B. D., and P. F. Worcester, 2000: Quantitative forecast skill for a quasi-geostrophic model, *J. Phys. Oceanogr.,* in preparation.

Dushaw, B. D., 2002: Mapping low-mode internal tides near Hawaii using TOPEX/POSEIDON altimeter data. *Geophys. Res. Lett.,* **29**, 10.1029/2001GL013944.

Dushaw, B. D., B. D. Cornuelle, P. F. Worcester, B. M. Howe, and D. S. Luther, 1995: Barotropic and baroclinic tides in the central North Pacific Ocean determined from long-range reciprocal acoustic transmissions. *J. Phys. Oceanogr.,* **25**, 631−647.

Dushaw, B. D., P. F. Worcester, B. D. Cornuelle, A. R. Marshall, B. M. Howe, S. Leach, J. A. Mercer and R. C. Spindel, 1996: Data Report: Acoustic Mid-Ocean Dynamics Experiment (AMODE). Tech. Rep. APL-UW TM 2-96, available from Applied Physics Laboratory, University of Washington, Seattle, WA, 275 pp.

Dushaw, B. D., G. D. Egbert, P. Worcester, B. Cornuelle, B. Howe, and K. Metzger, 1997: A TOPEX/POSEIDON global tidal model (TPXO.2) and barotropic tidal currents determined from long-range acoustic transmissions. *Prog. Oceanogr.*, **40**, 337−367.

Dushaw, B. D., and P. Worcester, 1998: Resonant diurnal internal tides in the North Atlantic. *Geophys. Res. Let.,* **25,** 2189−2192.

Egbert, G. D., and R. D. Ray, 2000: Significant dissipation of tidal energy in the deep ocean inferred from satellite altimeter data, *Nature,* **405,** 775−778.

Hendershott, M., 1981: Long waves and ocean tides. *Evolution of Physical Oceanography*, B. A. Warren and C. Wunsch, Eds., The MIT Press, 292−341.

Hendry, R. M., 1977: Observations of the semidiurnal internal tide in the western North Atlantic ocean. *Phil. Trans. R. Soc.,* **A286**, 1−24.

Holloway, P. E., and M. A. Merrifield, 1999: Internal tide generation by seamounts, ridges, and islands. *J. Geophys. Res.,* **104**, 25 937−25 951.

Kantha, L. H., and C. C. Tierney, 1997: Global baroclinic tides, *Prog. Oceanogr.,* **40,** 163−178.

Kay, S. M., and S. L. Marple, Jr., 1981: Spectrum analysis − a modern perspective. *Proc. IEEE,* **69,** 1380−1419.

Merrifield, M. A., P. E. Holloway, and T. M. Shaun Johnston, 2001: The generation of internal tides at the Hawaiian Ridge. *Geophys. Res. Lett.,* **28**, 559−562.

Mitchum, G. T., and S. M. Chiswell, 2000: Coherence of internal tide modulations along the Hawaiian Ridge. *J. Geophys. Res.* **105**, 28 653−28 661.

Munk, W., 1966: Abyssal recipes, *Deep-Sea Res.,* **13,** 707−730.

Munk, W., 2000: Once again: once again - tidal friction, *Prog. Oceanogr.,* **40,** 7−35.

Munk, W. H., and D. H. Cartwright, 1966: Tidal spectroscopy and prediction. *Phil. Trans. R. Soc. Lond.,* **A259**, 533−581.

Munk, W., P. Worcester, and C. Wunsch, 1995: *Ocean Acoustic Tomography.* Cambridge University Press, 433 pp.

Munk, W., and C. Wunsch, 1998: Abyssal Recipes II: energetics of tidal and wind mixing, *Deep-Sea Res.,* **45,** 1976−2000.

Pinkel, R., W. Munk, P. Worcester, B. D. Cornuelle, D. Rudnick, J. Sherman, J. H. Filloux, B. D. Dushaw, B. M. Howe, T. B. Sanford, C. M. Lee, E. Kunze, M. C. Gregg, J. B. Miller, J. M. Moum, D. R. Caldwell, M. D. Levine, T. Boyd, G. D. Egbert, M. A. Merrifield, D. S. Luther, E. Firing, R. Brainard, P. J. Flament, and A. D. Chave, 2000: Ocean mixing studied near Hawaiian Ridge. *Eos*, Trans. Am. Geophys. U., **81**, pp. 545,553.

Ray, R. D., and D. E. Cartwright, 2001: Estimates of internal tide energy fluxes from Topex/Poseidon altimetry: Central North Pacific. *Geophys. Res. Lett.,* **28,** 1259−1262.

Ray, R. D., and G. T. Mitchum, 1996: Surface manifestation of internal tides generated near Hawaii. *Geophys. Res. Lett.,* **23**, 2101−2104.

Ray, R. D., and G. T. Mitchum, 1997: Surface manifestation of internal tides in the deep ocean: Observations from altimetry and island gauges. *Prog. Oceanogr.,* **40**, 337−367.

Schureman, P., 1958: Manual of Harmonic Analysis and Prediction of Tides. *Spec. Publ. 98,*, U.S. Coast and Geod. Surv., U.S. Govt. Print. Off., Washington, D.C., 317 pp.

Urick, R. J., 1967: *Principles of Underwater Sound for Engineers.* McGraw-Hill, 342 pp.

Zang, X., and C. Wunsch, 1999: The observed dispersion relationship for the North Pacific Rossby wave motions. *J. Phys. Oceanogr.,* **29,** 2183−2190.
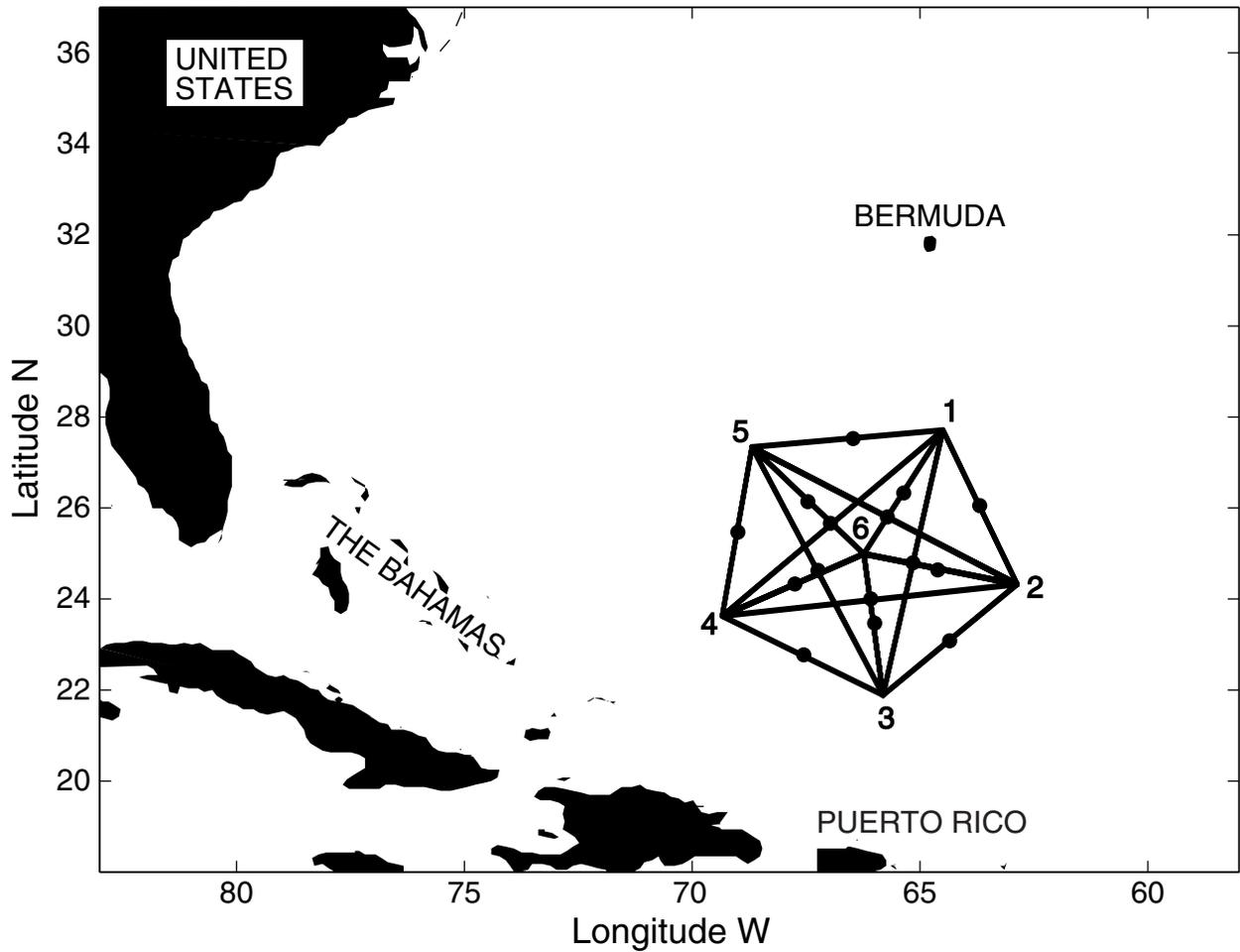
FIG. 1. Geometry of the AMODE acoustic tomography array located between Puerto Rico and Bermuda. The width of the array was about 670 km, and it consisted of six transceiver moorings, labeled 1−6. The array detected both semidiurnal and diurnal tidal signals of the lowest internal-wave mode. The dots at the midpoints of the acoustic paths indicate the fictional array of point measurements that is used for comparing the beam patterns of point and line-integral arrays.
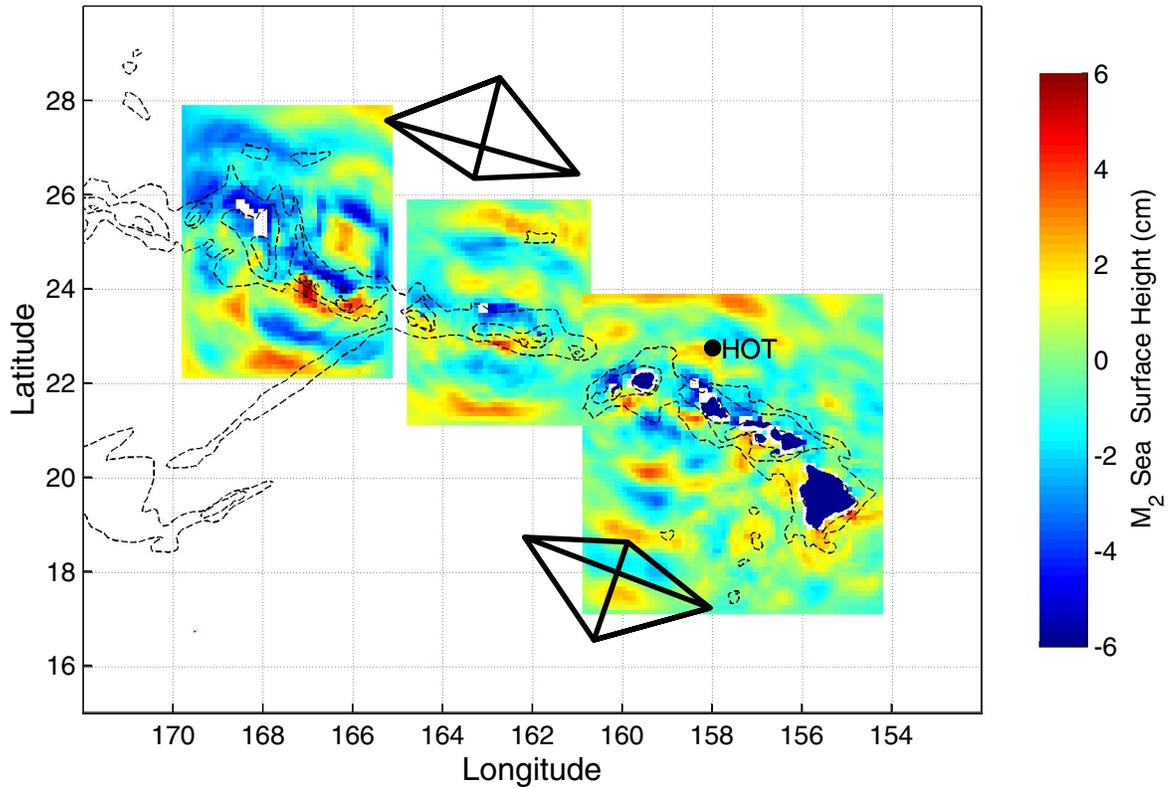
FIG. 2. Geometry of tomographic arrays deployed as part of the Hawaiian Ocean Mixing Experiment (HOME) in 2001. The colors show variations in sea surface height caused by the internal tide as predicted by a numerical ocean model in three distinct model domains (Merrifield et al. 2000). The variations in sea surface height are caused mainly by the lowest internal-wave modes. The tomography array is designed to detect the radiation of those modes.
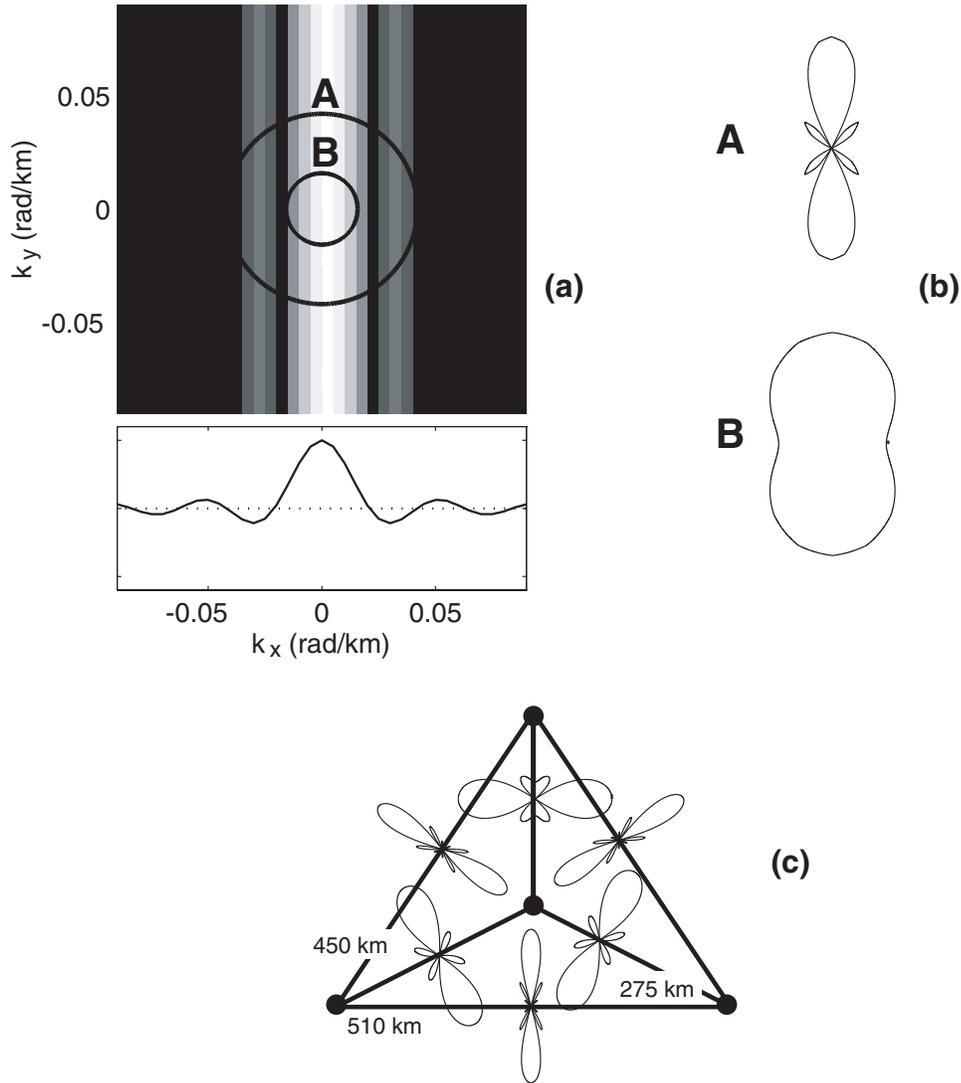
FIG. 3.   (a) Wavenumber filter for a zonally oriented acoustic path of 400-km length; this path gives a sinc filter for zonal wavenumbers and no filter for meridional wavenumbers. (b) The projection of the two-dimensional filter onto semidiurnal wavenumbers; **A** is the beam pattern (in polar coordinates), or the response of the line-integral antenna as a function of azimuthal angle, for semidiurnal radiation. The narrow beam pattern shows that the acoustic antenna has high directivity for semidiurnal wavenumbers. For the smaller diurnal wavenumbers, **B**, the acoustic antenna has less directivity. (c) The acoustic tomography array that was used for some of the simulations discussed in this paper. This array was designed to provide near-complete coverage of the wavenumbers of outgoing (upward in the figure) baroclinic-tide waves. The lengths of the acoustic paths are indicated.
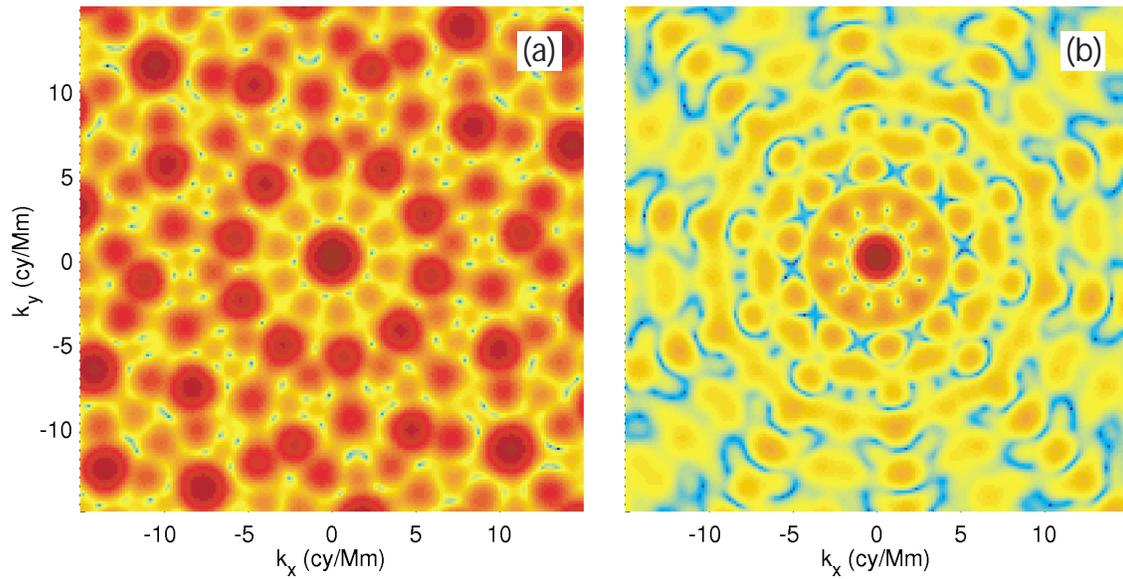
FIG. 4. Beam patterns for observing arrays consisting of (a) point and (b) line-integral measurements (see Fig. 1). The beam pattern of the array of point measurements has many sidelobes that are as strong as the main lobe. The elements of the line-integral array act coherently only for near-zero wavenumbers, but greater directivity is available. The different properties of these beam patterns result from the different sampling properties of the point and line-integral data.
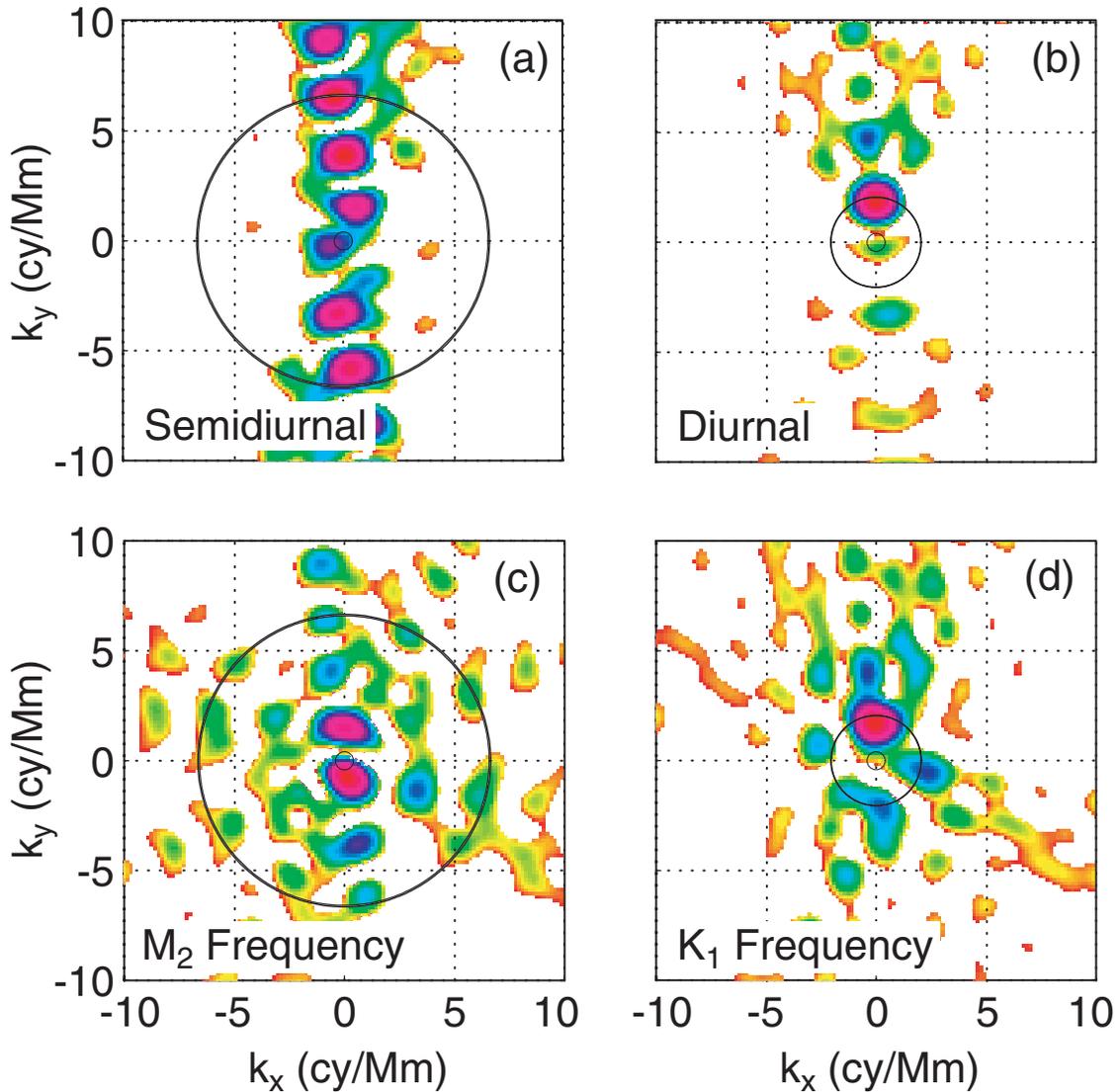
FIG. 5. Beam forming spectral estimates of simulated (a) semidiurnal and (b) diurnal northward wavenumbers observed by the AMODE tomographic array. For the simulated semidiurnal wavenumber, numerous sidelobes are found in the direction of propagation because only two zonal paths detect the wave. For the longer wavelength of a diurnal wave, the simulated incident wavenumber is well resolved. The actual spectral estimates using data obtained in 1991−2 during AMODE for the (c) M_2 and (d) K_1 constituent frequencies are comparable to the simulated spectra (see also Dushaw and Worcester 1998).

5 September 2002
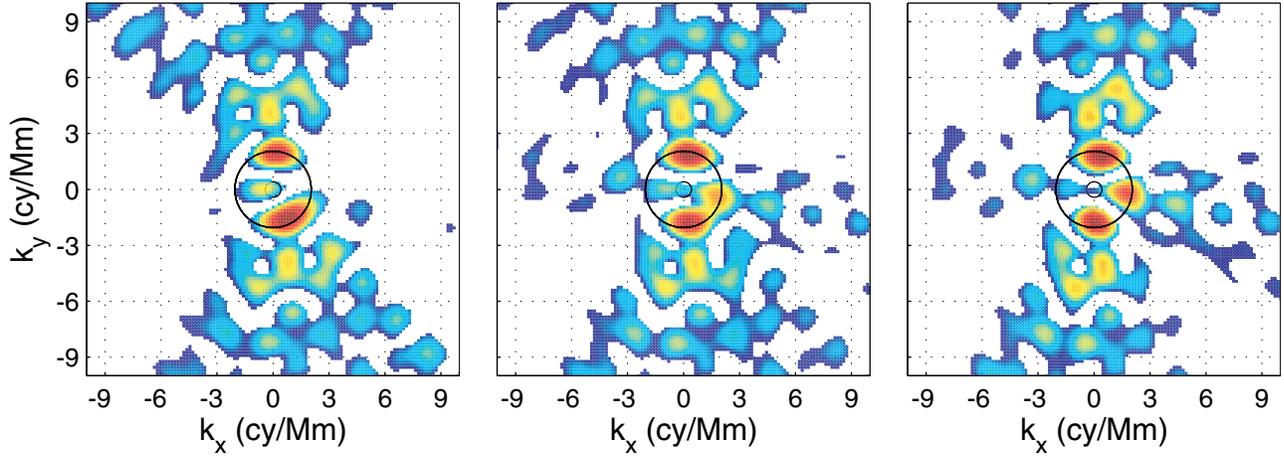
FIG. 6. The sensitivity of spectral estimates when several wavenumbers are present. Each panel is an estimate of the spectrum that would result when three diurnal wavenumbers are simultaneously incident on the AMODE array (Fig. 1). Two of the wavenumbers are meridional with equal in amplitude but opposite sign, so that they combine to form a standing wave. A third wavenumber is to the southeast with 30% smaller amplitude. Only the *phase* of the third wavenumber is different in the three spectra; from left to right this phase is 25°, 100°, and 165°. (See also Figs 5b and 5d.)
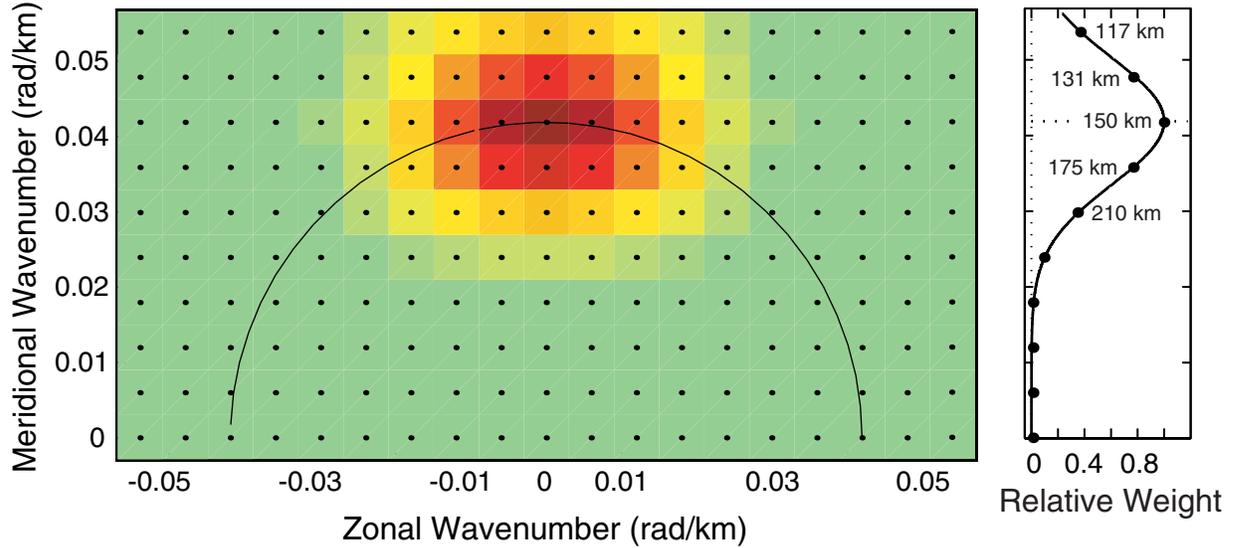
FIG. 7. Wavenumber spectrum used for simulating internal-tide fields. The wavenumbers of the simulated fields are approximately northward and centered on the theoretically expected wavenumber for semidiurnal radiation (the semicircle). The panel at right shows the section of the assumed spectrum when the zonal component of wavenumber is zero. The dots in both panels indicate wavenumbers that were used for the objective maps. A spectral peak with *ad hoc* width is used for the simulations; the "true" width is unknown.
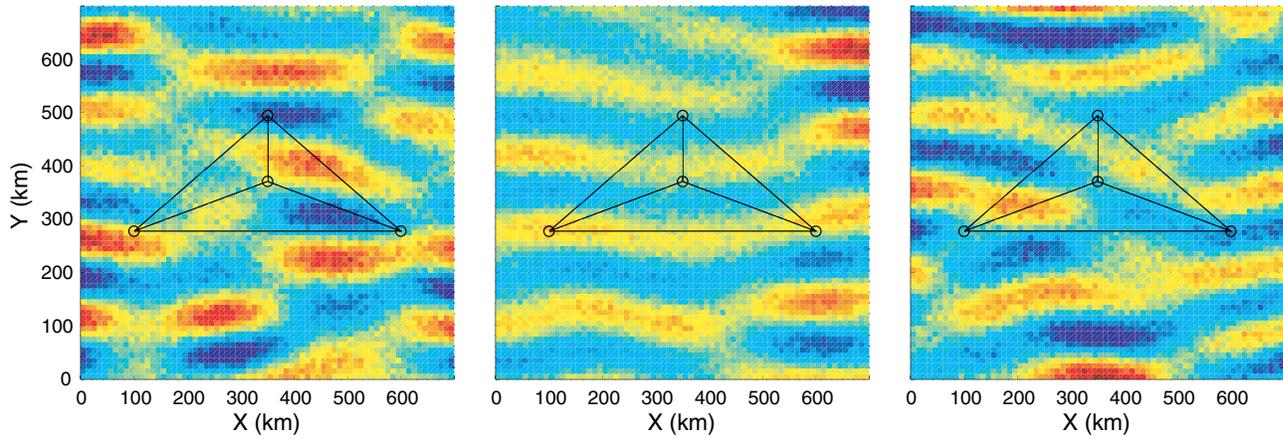
FIG. 8. Three realizations of the tidal field resulting from the spectrum shown in Fig. 7. These realizations are similar to the tidal fields around Hawaii calculated using a numerical ocean model (Fig. 2, Merrifield et al. 2000, Dushaw 2002). The realization in the panel at left may be compared with the objective maps shown in Figs. 9 and 11.
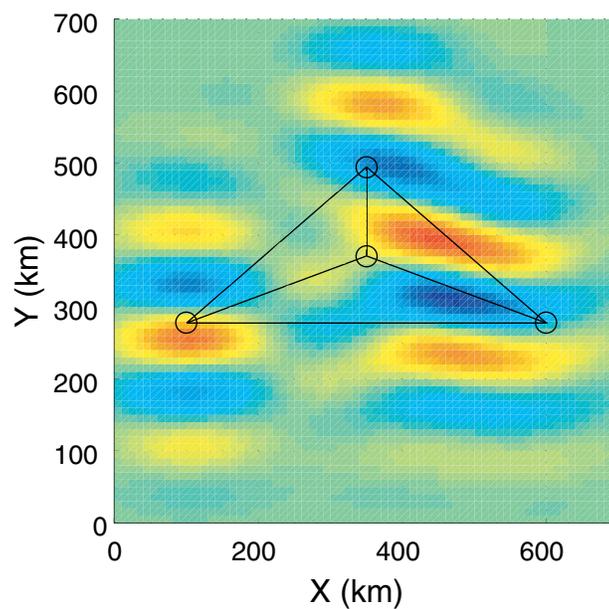
FIG. 9. An objective map of the tidal field based on line-integral data and point data obtained at the vertices of the array. The wavenumbers for this map were weighted according to the "true" spectrum (Fig. 7). The data were calculated from the simulated tidal field shown in the leftmost panel of Fig. 8.
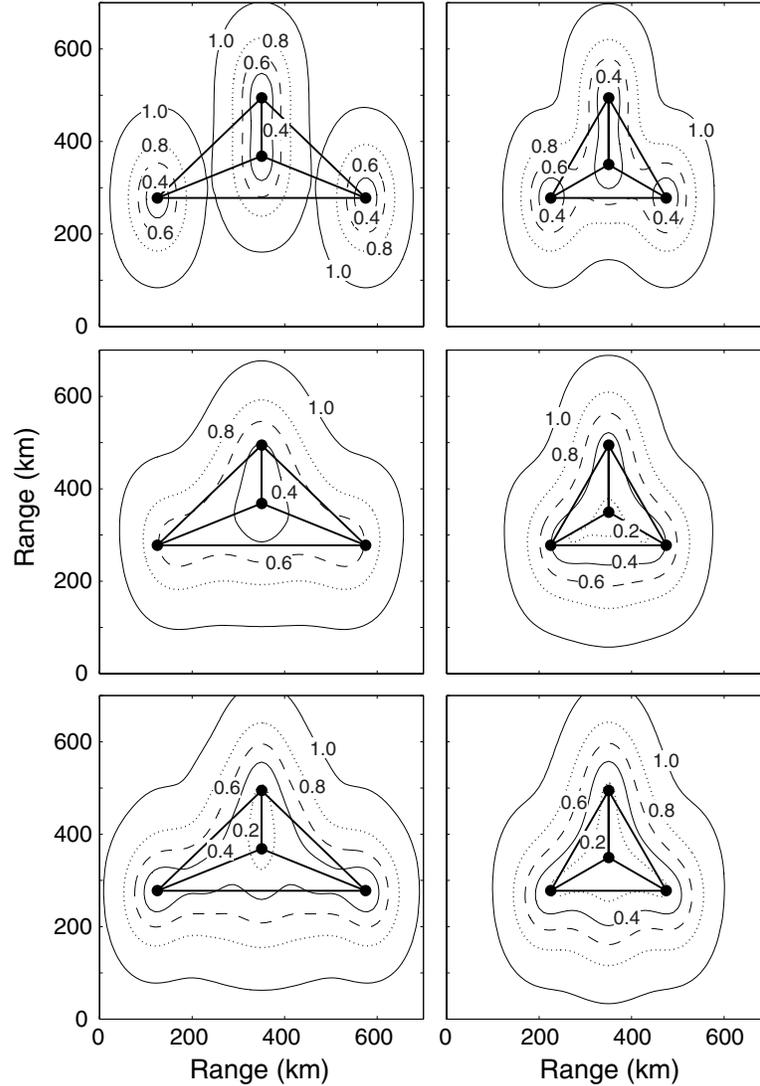
FIG. 10. Error maps resulting from the inversion for different array geometries and data types. The top panels show the error maps resulting when only point data at the array vertices are available. The middle panels show the results when using only the line-integral data, and the bottom panels when using both types of data. The array geometry shown in the panels to left is optimal for mapping the tidal fields when line-integral data are available, and the array geometry shown in the panels to right is optimal when only point data are available (see Fig. 12). The error maps are normalized to give an uncertainty of 1 when no data are available. Given the modeling assumptions, these sparse arrays can resolve the tidal fields to within an uncertainly of 20–40%.
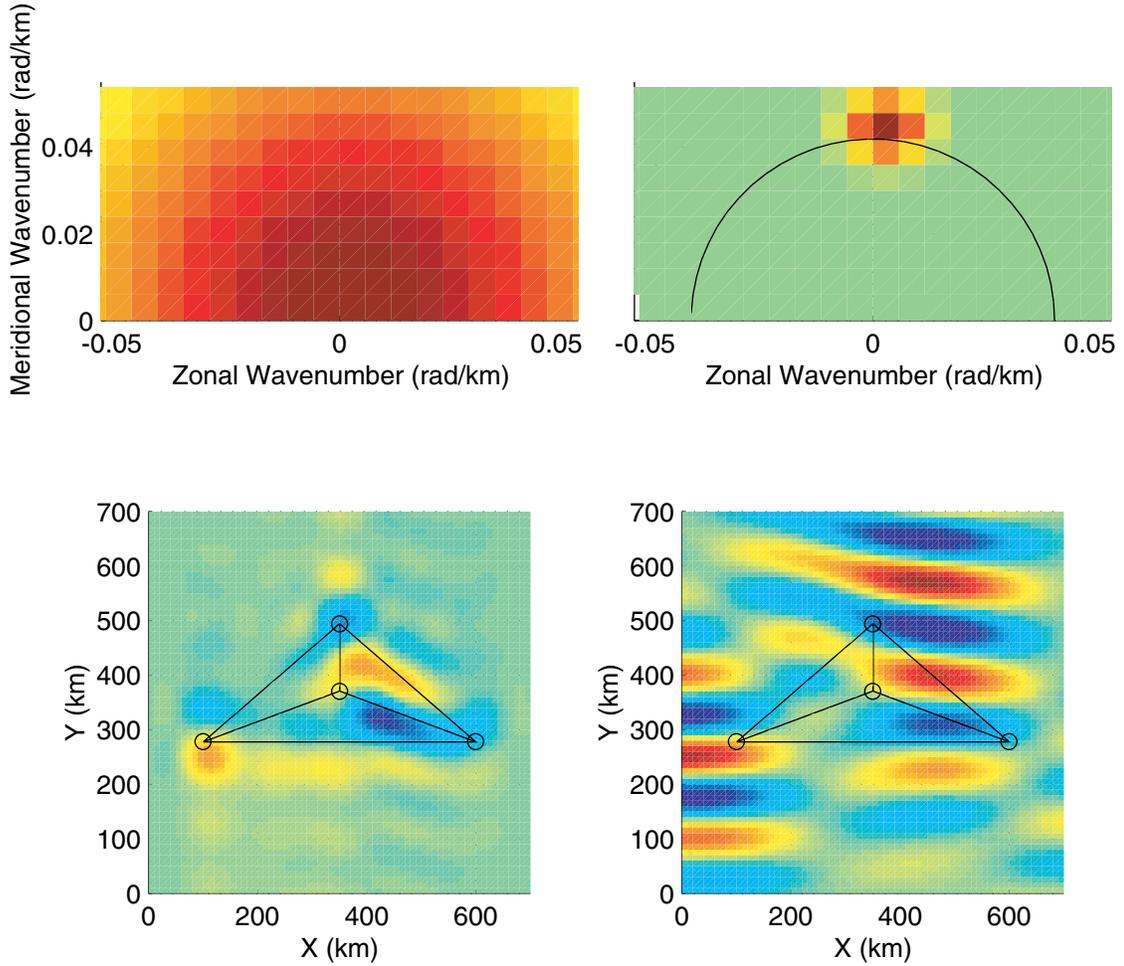
FIG. 11. Examples of maps of the tidal field when different *a priori* spectra are assumed. The top panels show the *a priori* spectra, and the bottom panels show the resulting maps. If the width of the spectral peak is assumed to be narrower, the resulting map will be more oscillatory. Compare these maps with the "true" map (Fig. 8) and the best objective map (Fig. 9).
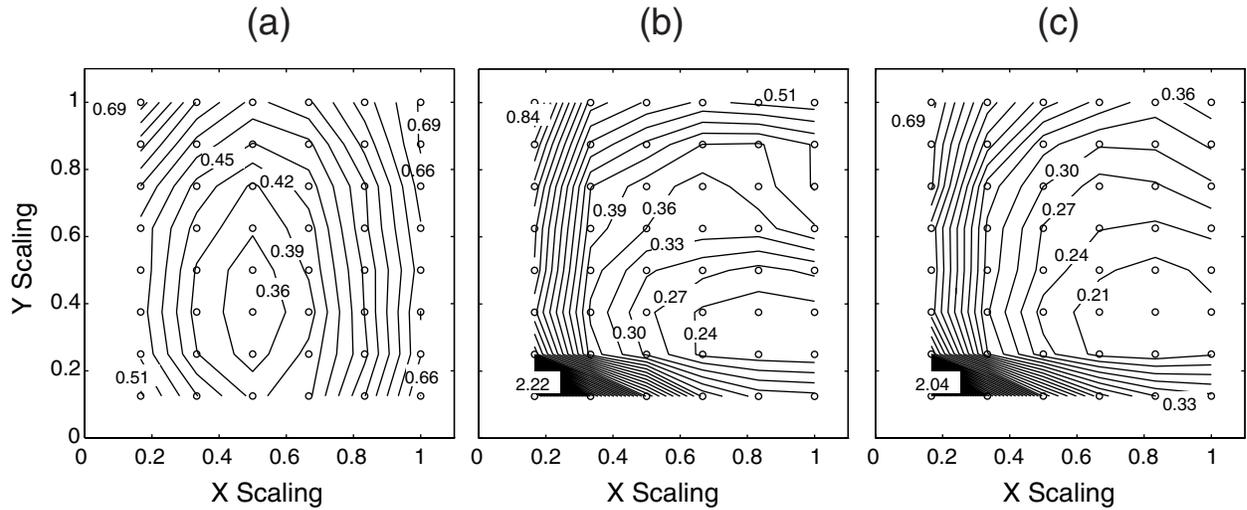
FIG. 12. Results of a search to determine the array size and shape that best resolve the simulated internal-tide fields. The "X and Y Scaling" show the zonal and meridional scaling of an equilateral triangle 500 km on a side. The open circles indicate the values for X and Y scales used. The contours show the mean-square misfit between the true fields and the inverse solution for the tidal fields over a 400-km-diameter circle using (21). The minimum misfits in each panel are consistent with the uncertainties of 20–40% determined from the error maps (Fig. 10). (a) The misfit of maps derived when using only point data from the array vertices. In this case, the best array for observing the tide is roughly equilateral with 250-km sides. The panels (b) and (c) show the misfit when line-integral and both data types are used, respectively. For these simulations, the line-integral data are better at resolving the tidal field than the point data.
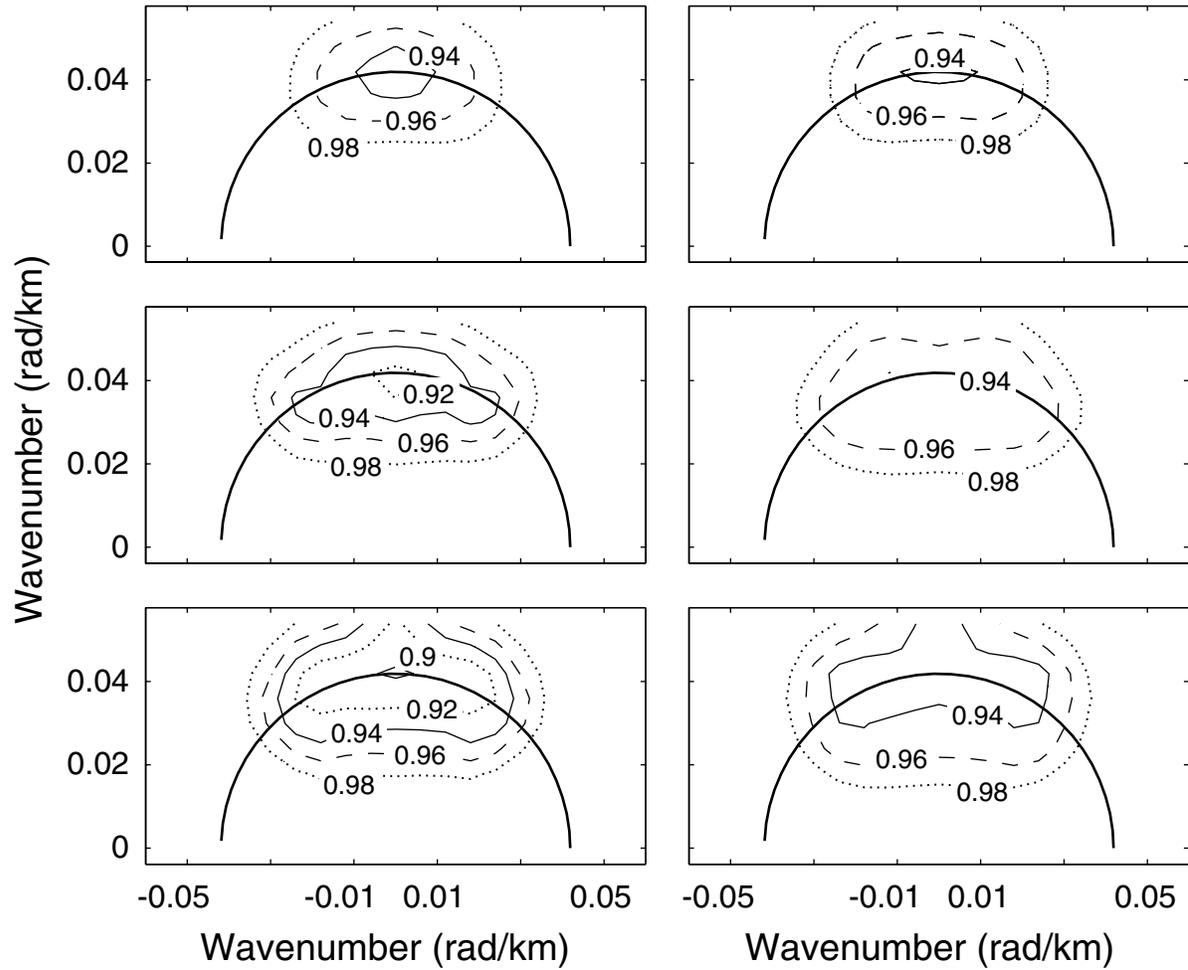
FIG. 13. Skill in resolving wavenumber amplitudes when using array shapes and data types corresponding to those shown in Fig. 10. No skill has a value of 1.0, and perfect skill has a value of 0.0. Because the observing array is sparse, its skill in resolving the individual amplitudes of the wavenumbers is poor.
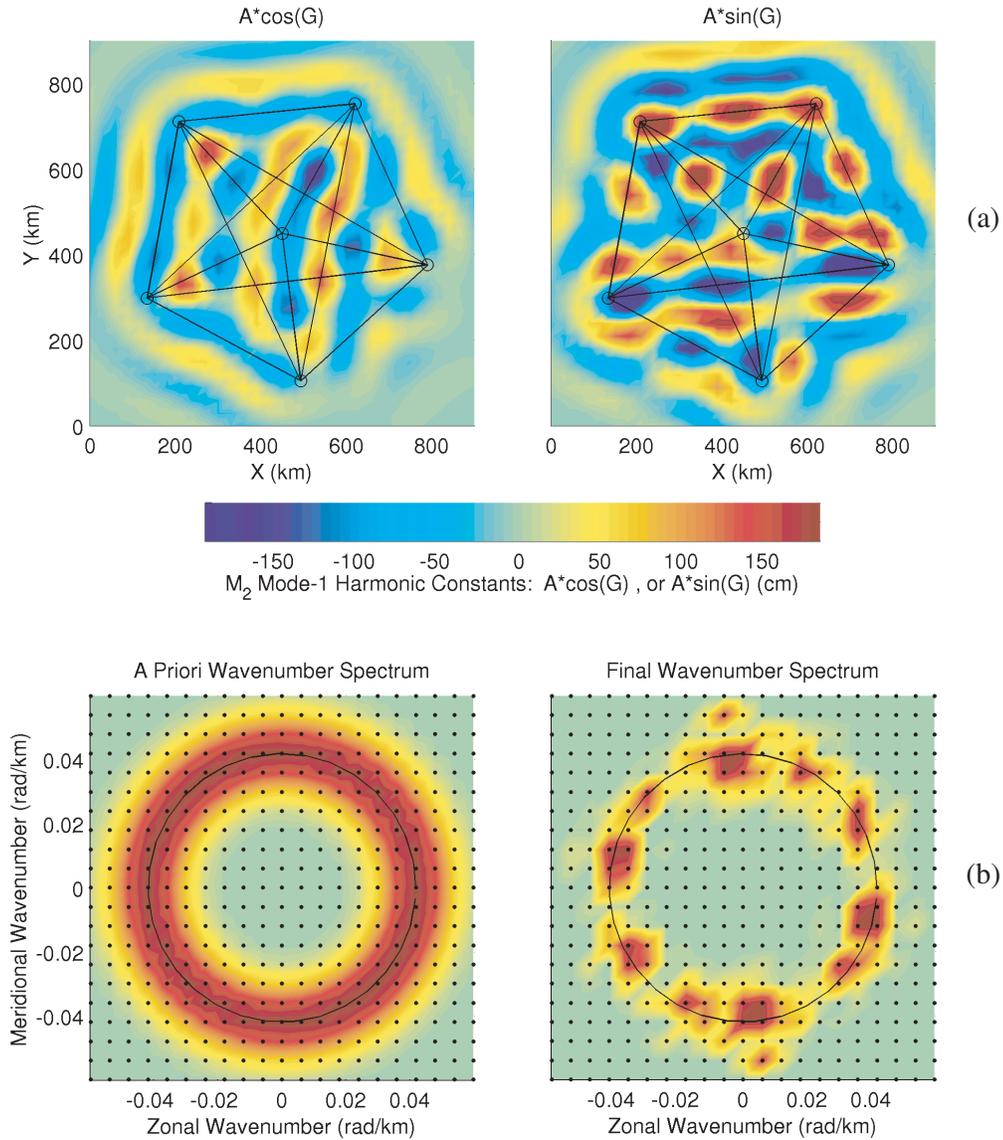
FIG. 14. (a) Maps of the M_2 internal-tide field observed by the AMODE array. The cosine component of the field (left) propagates northwest-southeast, while the sine component of the field (right) propagates meridionally. These solutions for the tidal field are standing waves that result from the sampling properties of the array and the symmetry of (b) the *a priori* wavenumber spectrum (left). The spectrum estimated from the objective map is also shown (right).